The Role of Eddy Transfer in Setting the Stratification and Transport of a Circumpolar Current

RICHARD KARSTEN,* HELEN JONES, AND JOHN MARSHALL

Department of Earth, Atmospheric, and Planetary Sciences, Massachusetts Institute of Technology, Cambridge, Massachusetts

(Manuscript received 21 July 2000, in final form 24 April 2001)

ABSTRACT

High resolution numerical experiments of a circumpolar current are diagnosed to study how lateral and vertical transfer of buoyancy by geostrophic eddies balances advection by a meridional circulation driven by surface wind stresses and buoyancy fluxes. A theory is developed in the framework of the ''residual circulation'' to relate the vertical and horizontal stratification set up to the transfer properties of eddies and the patterns of imposed wind and buoyancy forcing. Simple expressions are found for the depth of penetration, stratification, baroclinic transport, and residual circulation of the current. Finally, the ideas are applied to the Antarctic Circumpolar Current (ACC) and yield predictions for how its properties depend on wind and buoyancy forcing.

1. Introduction

In the southern oceans strong meridional gradients in air–sea buoyancy flux act to create a strong Polar Front along which the Antarctic Circumpolar Current (ACC) flows in thermal wind balance with the density gradients. Westerly winds also drive the ACC eastward and, through associated Ekman currents, induce an Eulerian meridional circulation (the Deacon cell) that acts to overturn isopycnals, enhancing the strong frontal region (see Fig. 1). The potential energy stored in the front is released through baroclinic instability, and the ensuing eddies play a fundamental role in the dynamical and thermodynamical balance of the ACC (see, e.g., McWilliams et al. 1978; Marshall 1981; Johnson and Bryden 1989; Gille 1997; Phillips and Rintoul 2000; and many others).

Traditionally, researchers have prescribed a stratification and studied the role of eddies spawned from it. But in collusion with imposed patterns of mechanical and buoyancy forcing, the eddies can set the stratification too. In this paper we argue that the eddies themselves are fundamental in setting the stratification—both in the horizontal and vertical.

In a companion paper, Marshall et al. (2002), we examined how a balance between eddy transport and surface forcing can set the stratification of a warm lens of fluid pumped down from the surface in an idealized laboratory setting. Here we extend that work to a circumpolar current. As sketched schematically in Fig. 1, we suppose that eddies transport buoyancy across the front releasing potential energy at a rate which balances its creation by mechanical and thermodynamic forcing at the surface. The final stratification of the front is then set by this balance. Thus, while stratification determines the eddies, the eddies in turn determine the stratification.

We begin by studying a series of numerical experiments that illustrate how a balance between eddies and surface forcing is established in a circumpolar current. We do not impose an initial stratification, but rather examine the stratification set up at equilibrium. The experiments are used to guide the development of a theory that predicts both the surface stratification of the circumpolar current and its depth of penetration in terms of the winds and buoyancy fluxes acting at the surface. The theory is developed in the framework of the transformed Eulerian mean (TEM: Andrews and McIntyre 1976), which reformulates the conservation equation in terms of a ''residual circulation'' that includes the effect of both mean flow and eddies.

The structure of the paper is as follows. In section 2, we present a description of the numerical simulations. In section 3, we develop and interpret simulations in terms of a simple analytical system that can be solved to give the stratification. In section 4, we discuss the ramifications of the theory for the ACC, demonstrating how surface forcing determines the structure and transport of the current as well as the sense of the residual circulation. In section 5, we discuss the results and conclude.

* Current affiliation: Department of Mathematics and Statistics, Acadia University, Wolfville, Nova Scotia, Canada.

Corresponding author address: Richard Karsten, Department of Mathematics and Statistics, Acadia University, Wolfville, NS B0P 1X0, Canada.

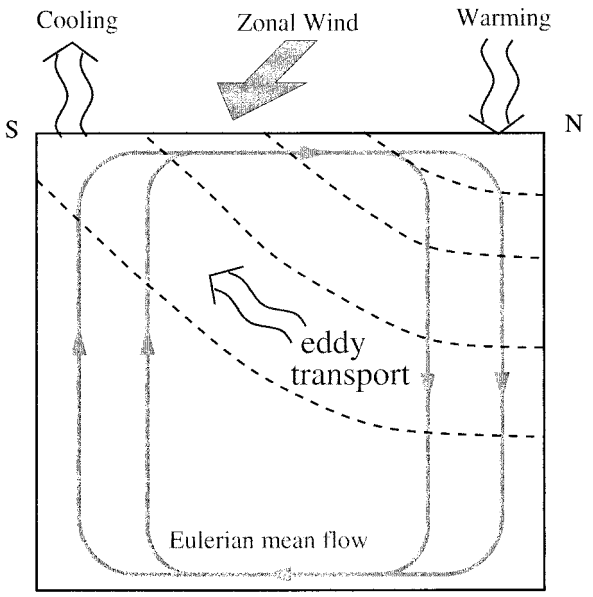

FIG. 1. A sketch of the balance that establishes the stratification of a circumpolar current. The dashed lines represent tilted isopycnals, the solid curves the streamlines of the mean wind-driven overturning. The overturning circulation together with differential heating—cooling in the south near Antarctica and warming in the subtropics—act to overturn isopycnals creating the Polar Front. This front becomes unstable and the resulting eddy transports balance the surface forcing establishing a statistically steady state.

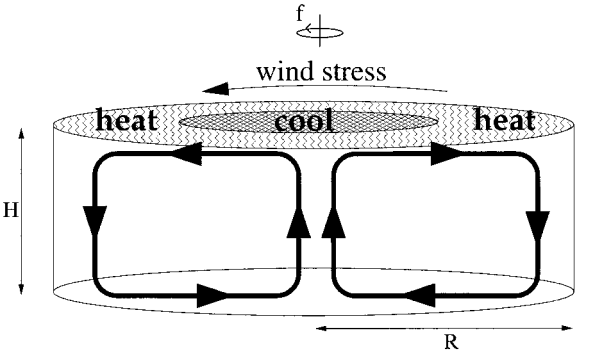

FIG. 2. The domain used in our numerical simulations. A rotating cylinder of fluid of radius R and depth H is forced at the surface by a wind stress and patterns of heating and cooling. The wind stress drives a meridional overturning as indicated by the arrows.

2. Numerical simulations

a. The experiments

We now describe numerical solutions of a circumpolar current designed to study the balance between eddy transport and surface forcing. Because this work was inspired by laboratory studies (see Marshall et al. 2002), and in subsequent work will be tied to further laboratory experiments, we set up a current in a cylindrical domain of radius R and depth H (see Fig. 2) on an f plane. Details of the experiments studied here are given in Table 1. Our domain approximates a polar cap and allows the realization of a circumpolar current. The MITgcm (Marshall et al. 1997a,b) was used.

The model resolution is sufficient to represent both vertical and horizontal structure of the front and eddies that develop. For a typical front, the horizontal grid size is roughly one fifth the Rossby deformation radius. This allows the details of the baroclinic waves and eddies to be captured accurately. In the vertical, the grid size is sufficiently small to crudely capture the surface Ekman layer and more than sufficient to resolve the vertical stratification of the front.

For simplicity, the bottom is flat and there are no land masses. While bottom topography is no doubt important in a detailed model of the ACC (Munk and Palmén 1951), it is ignored here in order to obtain a clear picture of the balances involved in a symmetric annular region. Similarly, the ACC is influenced by the interaction of the circumpolar flow allowed through Drake Passage and the gyre-like flows in the Atlantic and Pacific. However, we concur with studies (Gnanadesikan and Hallberg 2000; Gent et al. 2001; Tansley and Marshall 2001) that have shown that it is the circumpolar flow through Drake Passage and not the Sverdrupian gyre flow that determines ACC transport. Our model thus only examines circumpolar flow. The simplicity of our geometry allows us to diagnose the flow in terms of azimuthal averages; we will refer to the azimuthal direction as zonal and the radial direction as meridional.

1) PATTERNS OF MECHANICAL AND THERMAL FORCING

Beginning with a resting homogeneous fluid, we force at the surface with an azimuthal wind stress that generates a meridional overturning as sketched in Fig. 2. We include diffusion of momentum, ν, to support Ekman layers at both the surface and the bottom. The surface is forced by a zonal wind stress per unit density,

TABLE 1. The forcing and diagnostics for the numerical simulations that have been run. The depths h_e and strengths Δb of the fronts have been normalized by the depth of the domain, H, and the buoyancy at the center of the domain, $b_{r=0}$, respectively. The first experiment listed is our reference experiment. For all the experiments $R = 60$ and $H = 15$ cm with a horizontal and vertical resolution of 1 and 0.5 cm, respectively. In all experiments there is Laplacian diffusion of temperature and momentum with diffusivities of 1×10^{-7} m^2 s^{-1} and 5×10^{-6} m^2 s^{-1}, respectively.

τ_0 $\times 10^{-5}$ (m^2 s^{-2})	B_0 $\times 10^{-7}$ (m^2 s^{-3})	f (s^{-1})	h_e/H	$\Delta b/b_{r=0}$
0.48	**2.47**	**0.75**	**0.23**	**5.11**
0.48	4.91	0.75	0.17	11.0
0.48	1.23	0.75	0.32	6.20
0.84	2.47	0.75	0.28	6.93
1.68	2.47	0.75	0.47	4.36
3.36	2.47	0.75	0.98	1.60
0.16	2.47	0.25	0.20	4.35
0.96	2.47	1.50	0.32	9.78

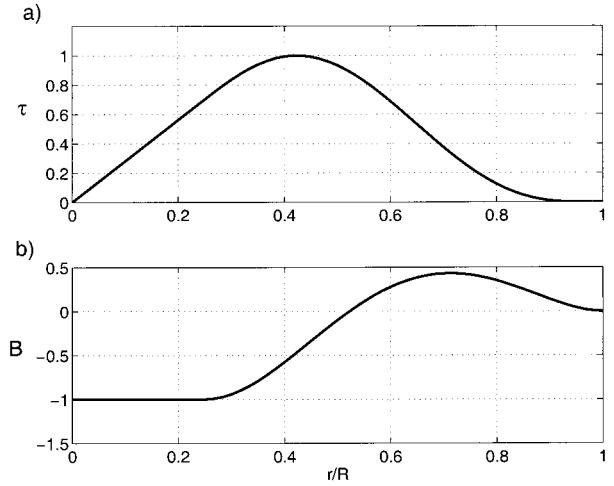

FIG. 3. (a) The nondimensional wind stress, $\tau(r)$, and (b) the surface buoyancy forcing, $B(r)$, used in the numerical simulations. Multiplying these nondimensional functions by a wind stress scale, τ_0, and a buoyancy flux scale, B_0, (see Table 1) gives the applied forcing for a given simulation. The buoyancy forcing vanishes at $r = r_0$ with $r_0/R = 0.51$.

$\tau(r)$, which vanishes at $r = 0, R$ (see Fig. 3). A mean circulation develops according to Ekman theory (see Pedlosky 1987) with streamfunction

$$\overline{\Psi}_{\text{Ek}} = \left(\frac{\tau}{f}\right)\mathcal{E}(z), \tag{1}$$

and velocities

$$\overline{w}(r, z) = \frac{1}{r}\frac{\partial}{\partial r}(r\overline{\Psi}_{\text{Ek}}), \qquad \overline{v}(r, z) = -\frac{\partial\overline{\Psi}_{\text{Ek}}}{\partial z}, \tag{2}$$

where $\mathcal{E}(z)$ is a vertical structure function associated with the mechanically driven circulation and r is the radius. Outside the Ekman layers, $\mathcal{E}(z) = 1$ and the flow is purely vertical, as sketched in Fig. 1. Within the surface Ekman layer there is meridional Ekman transport of magnitude

$$v_{\text{Ek}} = \frac{\tau}{f}. \tag{3}$$

There is also a bottom Ekman layer with an equal transport but of opposite sign to the surface. Although the Ekman transport plays an essential role in the dynamics, our theory is insensitive to the exact structure within the Ekman layer.

Once the fluid is spun up, a buoyancy forcing is applied that heats an exterior ring while cooling at the center (see Fig. 3). The forcing is chosen so that no net buoyancy is added to the system.[1] A convective adjustment scheme is used to eliminate the unstable stratification that forms when the surface is cooled.

2) NUMERICAL SOLUTIONS

In Fig. 4, we illustrate the evolution of a typical numerical circumpolar current; parameter values are those of our reference experiment (see Table 1). As the heating begins, a warm ring of fluid forms (see $t = 75$—after 75 rotation periods). This fluid is pumped down to depth and forms a temperature front (as seen in the zonal mean cross section at $t = 75$) with an associated thermal wind current. The current becomes unstable, and initial small waves grow rapidly into eddies. As time proceeds, the front gets warmer and deeper while the eddies grow larger. The action of the eddies allows the front to spread across the tank (compare the zonal mean at $t = 150$ to that at $t = 75$). Eventually (at $t = 1500$) we reach a quasi-steady state in which a strong, deep front supports a vigorous field of large eddies. The eddies sweep fluid across the front, transporting warm water inward and cooler water outward. This exchange reaches such a magnitude that it can balance the surface forcing.

In Fig. 5, we plot the time evolution of the temperature anomaly at a point under the heating ($r/R = 2/3$) for all vertical levels in the model. Initially, we see a rapid rise in temperature as the heating begins. Subsequently, as eddies begin to form, the temperature rises at a lower rate. The lens continues to warm and deepen while eddies continue to grow. Finally, after the eddy transport has become sufficiently large, the temperature levels off to a quasi-steady value.

In Fig. 6, we plot the time and zonal mean of the quasi-steady temperature anomaly and current. Horizontal variations in the temperature are concentrated in a front where the buoyancy forcing and the wind-driven vertical velocity change sign, $r = r_0$. The front extends to roughly half the depth of the fluid, so little variation in temperature is seen at the bottom. The corresponding baroclinic zonal flow is a surface trapped current centered at $r = r_0$.

To make theoretical progress we assume that the mean buoyancy, $\overline{b}$, is separable and has an exponential profile in the vertical:

$$\overline{b} = M(r)\exp(z/h_e), \tag{4}$$

where $M(r)$ is the horizontal structure and h_e is the e-folding depth. In Fig. 7, we plot the zonally averaged, vertical profiles through the core of the front ($r/R = 0.3$ to 0.8) normalized by their surface value. A best fit exponential curve to the average of the vertical profiles is also plotted. The curves—a total of 32 are plotted—are nearly indistinguishable indicating that (4) captures the spatial variation more than adequately. It is interesting to note that an exponential profile for the ACC is also supported by observations (Marshall et al. 1993) and Fine Resolution Antarctic Model results (Killworth 1992; Krupitsky et al. 1996). The e-folding depth of the

[1] In this paper we make no distinction between heat and salinity fluxes. To simplify our discussion we refer only to temperature and heat fluxes.

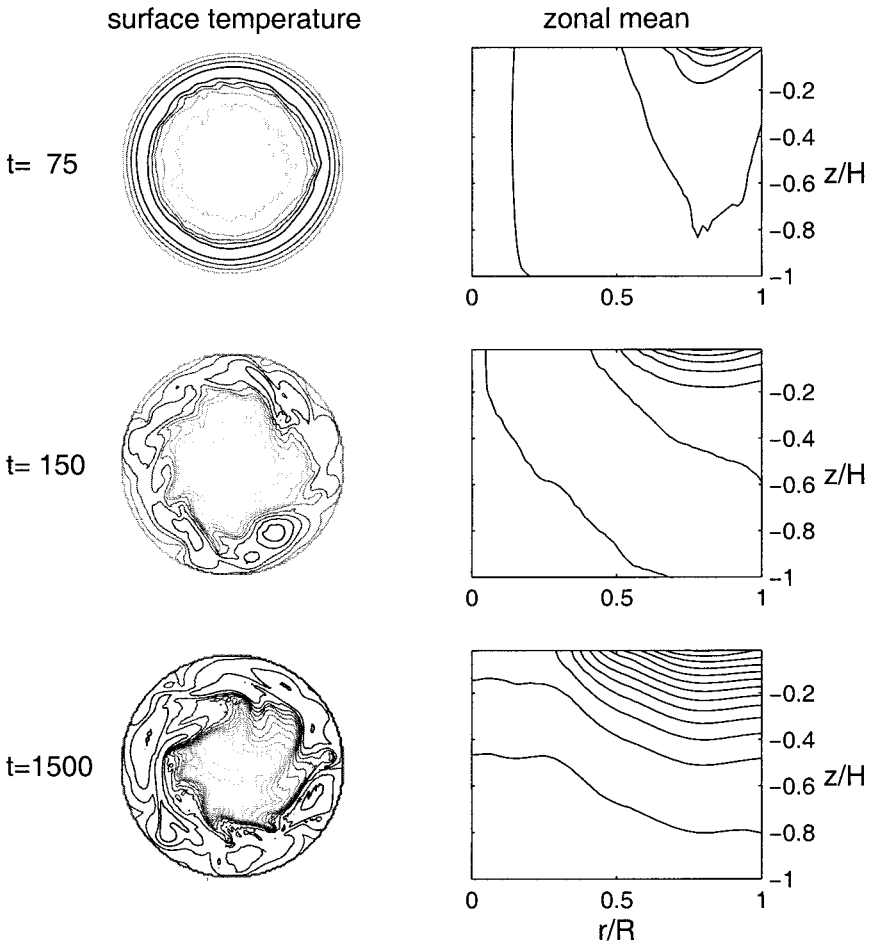

FIG. 4. Results from a typical numerical simulation. Surface temperature is plotted on the left and a cross section of the zonal mean temperature on the right. The time for each plot is given in rotation periods. The contours interval is 1°C with lighter contours for cooler temperatures.

vertical profile, h_e, gives a measure of the depth of the front. To quantify the lateral gradient we define the strength of the front Δb as the difference in buoyancy across it at the surface:

$$\Delta b \equiv M(R) - M(0) = b(r = R) - b_{r=0}, \qquad (5)$$

where

$$b_{r=0} \equiv M(0) \qquad (6)$$

is the minimum surface buoyancy.

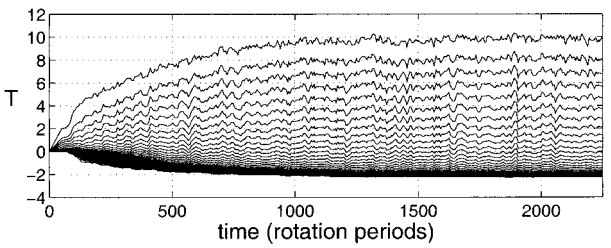

FIG. 5. Time evolution of the temperature anomaly, T, in °C, at $r/R = 2/3$.

A series of experiments was run with varying surface forcing and rotation rates, as summarized in Table 1. The resulting equilibrium e-folding depth and buoyancy strength diagnosed from each experiment is also tabulated.

b. Buoyancy budgets

By diagnosis of the numerical simulations, we can determine buoyancy budgets that reveal the importance of various fluxes in the model. For example, consider the buoyancy budget of a cylinder of variable radius $0 \leq r \leq R$ extending over the entire depth of the fluid (see Fig. 8a). At equilibrium, the net buoyancy in the cylinder is conserved. Therefore the fluxes out of the cylinder, due to the surface buoyancy loss (we are cooling at the center) and Ekman transport (which is outward since the fluid moving outward at the surface is warmer than the fluid moving inward at the bottom), must balance inward fluxes due to horizontal eddy fluxes. In Fig. 8b, we plot these three terms versus the normalized

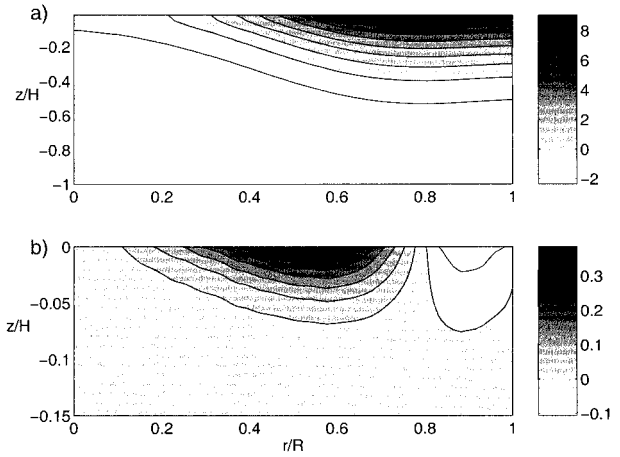

FIG. 6. Cross sections of the mean temperature anomaly (a) and mean thermal wind velocity (b). The temperature is in °C, while the velocity is in cm s^{-1}.

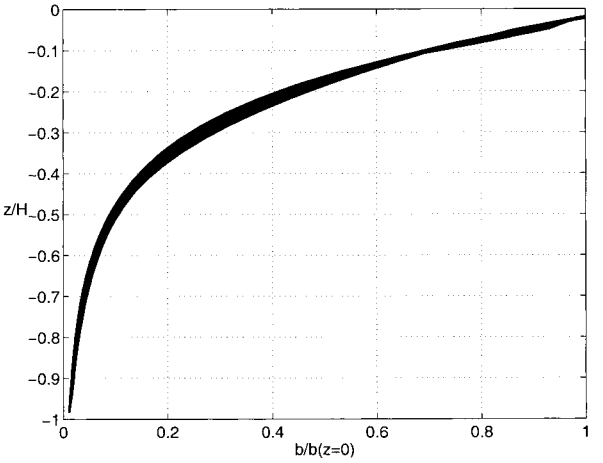

FIG. 7. The 31 vertical profiles of buoyancy in the core of the current, normalized by their surface values, and a best fit exponential.

radius of the cylinder, r/R, for the reference simulation. The total flux is nearly zero, indicating that we have a balance. As such, other possible fluxes, for example explicit horizontal diffusion, play at most a minimal role. We also see that the primary balance is between the eddy transport and Ekman transport, with the surface heating playing a secondary role.

Next, we consider the buoyancy budget over a disc extending the full radius of the domain R with variable depth $-H < z < 0$ (see Fig. 9a). The downward flux out of the disc consists of Ekman pumping and vertical diffusion, while the upward flux into the disc is achieved by eddies. In Fig. 9b, we plot the various terms as a function of normalized depth, z/H, for the reference simulation. Once again, the total flux is near zero (except at the surface) and the primary balance is between the Ekman transport and the eddy transport.

c. The eddy fluxes

The buoyancy budgets clearly show the central role played by eddy fluxes in setting up the ambient stratification. In order to develop a theoretical understanding we now examine the nature of the fluxes in more detail.

Let us suppose that the horizontal eddy flux is directed downgradient with an eddy diffusivity K defined by

$$\overline{v'b'} = -K\frac{\partial \overline{b}}{\partial r}. \tag{7}$$

The diagnosed eddy diffusivity is not constant in our numerical simulations but has a pronounced maximum near the surface. This can be seen in Fig. 10a where we plot the vertical profile of the horizontally averaged K for the reference experiment. The eddy diffusivity is roughly constant in the interior but increases by some 30% toward the surface. This is a robust pattern observed in all our experiments.

Hence, we write the net lateral buoyancy flux thus:

$$\int_{-H}^{0} \overline{v'b'}\, dz = -\int_{-H}^{0} K(z)\frac{\partial \overline{b}}{\partial r}\, dz$$
$$= -(1 + \epsilon)K_I \int_{-H}^{0} \frac{\partial \overline{b}}{\partial r}\, dz, \tag{8}$$

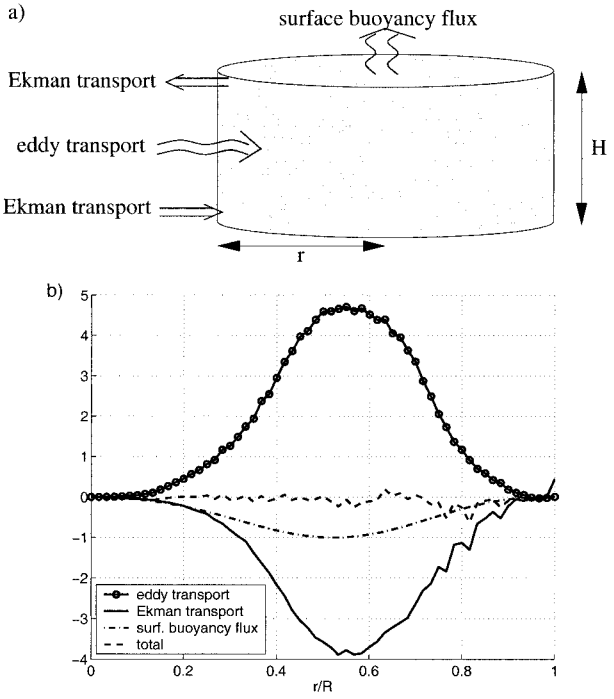

FIG. 8. (a) A cylinder of variable radius, $0 < r < R$, and extending the full depth of the tank, H. At equilibrium, the outward buoyancy fluxes due to surface buoyancy loss and the net Ekman transport are balanced by inward eddy buoyancy fluxes. (b) The buoyancy budget for the cylinder shown in (a) as diagnosed from the reference numerical simulation. A flux into the cylinder is considered positive. The values are normalized by the net surface buoyancy cooling over the disc of radius r_0, i.e., $\int_0^{r_0} Br\, r$.

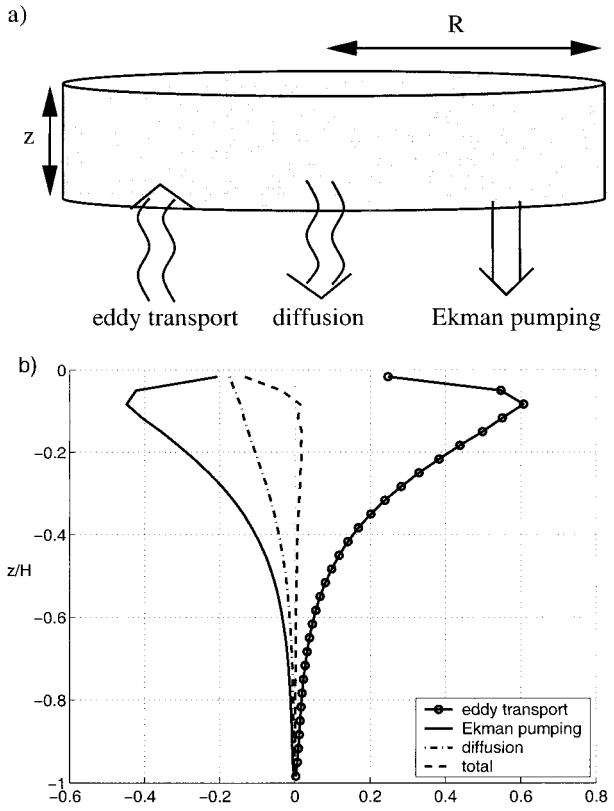

FIG. 9. (a) A disk extending the full radius of the tank and down to a variable depth $-H \leq z \leq 0$. At equilibrium the downward buoyancy fluxes due to Ekman pumping and diffusion are balanced by upward eddy buoyancy fluxes. (b) The buoyancy budget for the disk shown in (a) as diagnosed from the reference numerical simulation. A flux into the disc is considered positive. The values are normalized as in Fig. 8.

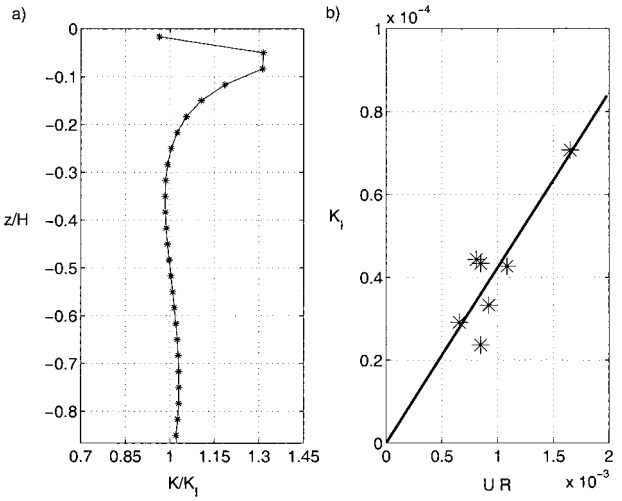

FIG. 10. (a) The vertical profile of eddy diffusivity as diagnosed from the reference numerical simulation using (7). Values are normalized by the interior value of the diffusivity, K_I. (b) The diagnosed value of K_I vs the formula $U \times R$ for all experiments (stars). The slope of the best fit line gives us the eddy efficiency coefficient $c_e = 0.043$.

where K_I is the value of the diffusivity in the interior and ϵ is a small positive constant. For the reference experiment we find that $\epsilon = 0.11$ (see Fig. 10).

We assume, as in Marshall et al. (2002), that the eddy diffusivity is proportional to the average surface thermal wind, U, multiplied by a transfer length scale, L_m; that is,

$$K_I = c_e U L_m, \tag{9}$$

where c_e is the eddy efficiency parameter and the average surface thermal wind is given by

$$U = \frac{\int_0^R u(r, 0)\, dr}{R} = \frac{1}{f_0 R} \int_0^R \int_{-H}^0 \frac{\partial \bar{b}}{\partial r}\, dz\, dr. \tag{10}$$

The numerical simulations suggest that the eddies will cascade to the largest scale supported by the geometry of the tank; that is, $L_m = R$.

Relation (9) finds support in the numerical simulations. In Fig. 10b, we plot the K_I diagnosed from the simulations versus $U \times R$. The data fall roughly on a straight line with the slope giving the eddy efficiency parameter $c_e = 0.043$, somewhat smaller than that reported in Marshall et al. (2002), but consistent with the values found by Visbeck et al. (1996), Whitehead et al. (1996), and Jones and Marshall (1997).

Finally we consider the surfaces along which the eddy flux is directed. If the eddy flux has a diapycnal component, then it is useful to write

$$\overline{w'b'} = \mu s_\rho \overline{v'b'}, \tag{11}$$

where the magnitude of the diapycnal flux is controlled by μ, the ratio of the slope along which the eddies transfer to the isopycnal slope s_ρ, given by

$$\mu = \left(\frac{\overline{w'b'}}{\overline{v'b'}}\right)\left(\frac{1}{s_\rho}\right). \tag{12}$$

If the eddy flux is purely along isopycnals, that is, adiabatic, then $\mu = 1$. Treguier et al. (1997) and Marshall (1997) suggest eddies are adiabatic except in the mixed layer in which the density is vertically homogeneous and eddy transport is purely horizontal and thus purely diapycnal. On diagnosing our numerical simulations we find that μ is close to one in the interior but decreases sharply to zero toward the surface.

3. Theoretical model

a. Transformed Eulerian mean formulation

We now examine the zonally and temporally averaged equations in the statistically steady state. For incompressible flow, conservation of buoyancy can be written as

$$\overline{v}\frac{\partial \overline{b}}{\partial r} + \overline{w}\frac{\partial \overline{b}}{\partial z} + \frac{1}{r}\frac{\partial}{\partial r}(r\overline{v'b'}) + \frac{\partial}{\partial z}\overline{w'b'} = \frac{\partial B}{\partial z} + \kappa\frac{\partial^2 \overline{b}}{\partial z^2}, \quad (13)$$

where v is the radial velocity and w is the vertical velocity. In (13) the variables have been separated into mean (zonal and time) quantities, $\overline{b}$, and perturbations from this mean, b'. The buoyancy forcing has been written as the divergence of a buoyancy flux, B, with a positive value indicating a flux of buoyancy into the fluid. We have included vertical diffusion but, guided by Fig. 8, horizontal diffusion has been neglected.

It is very instructive to rewrite the equations in terms of a residual mean meridional circulation (see Andrews et al. 1987 for a background discussion). Following Held and Schneider (1999), we introduce the residual mean streamfunction in terms of vertical eddy fluxes and write

$$\Psi_{\text{res}} = \overline{\Psi}_{\text{Ek}} + \Psi^*, \quad (14)$$

where $\overline{\Psi}_{\text{Ek}}$ is given by (1) and Ψ^* by

$$\Psi^* = -\frac{\overline{w'b'}}{\overline{b}_r}, \quad (15)$$

which vanishes at the surface and bottom of the fluid.

The residual mean meridional circulation is given by

$$\overline{v}_{\text{res}} = -\frac{\partial \Psi_{\text{res}}}{\partial z}, \qquad \overline{w}_{\text{res}} = \frac{1}{r}\frac{\partial}{\partial r}(r\Psi_{\text{res}}), \quad (16)$$

where the subscript res denotes ''residual.'' Noting that the advecting velocities in the Eulerian balance (13) are ageostrophic and associated with the directly wind-driven flow, $\overline{\Psi}_{\text{Ek}}$, we eliminate them in favor of Ψ_{res} using (14), to arrive at an alternative form of (13):

$$\frac{1}{r}J(r\Psi_{\text{res}}, \overline{b}) = \frac{\partial B}{\partial z} + \kappa\frac{\partial^2 \overline{b}}{\partial z^2} - \frac{1}{r}\frac{\partial}{\partial r}[r(1-\mu)\overline{v'b'}], \quad (17)$$

where $J(r\Psi_{\text{res}}, b) = (r\Psi_{\text{res}})_r b_z - (r\Psi_{\text{res}})_z b_r$ and μ is given by (12). Equation (17) states that the advection of buoyancy by the residual recirculation is induced by surface forcing, vertical diffusion, and a diapycnal eddy flux.

To arrive at (17) from (13) we decomposed the eddy fluxes $(\overline{v'b'}, \overline{w'b'})$ into an along isopycnal component $(\overline{w'b'}/s_\rho, \overline{w'b'})$ and the remaining horizontal component $(\overline{v'b'} - \overline{w'b'}/s_\rho, 0)$. The divergence of the along isopycnal component is then written as an advective transport

$$\nabla \cdot \left(\frac{\overline{w'b'}}{s_\rho}, \overline{w'b'}\right) = \overline{v}^*\overline{b}_r + \overline{w}^*\overline{b}_z = \frac{1}{r}J(r\Psi^*, b).$$

The divergence of the diapycnal (horizontal) eddy flux, leads to the last term on the right-hand side of (17). If the eddy flux is solely along isopycnals, $\mu = 1$, then the diapycnal horizontal component vanishes and the advective transport captures the entire eddy flux.

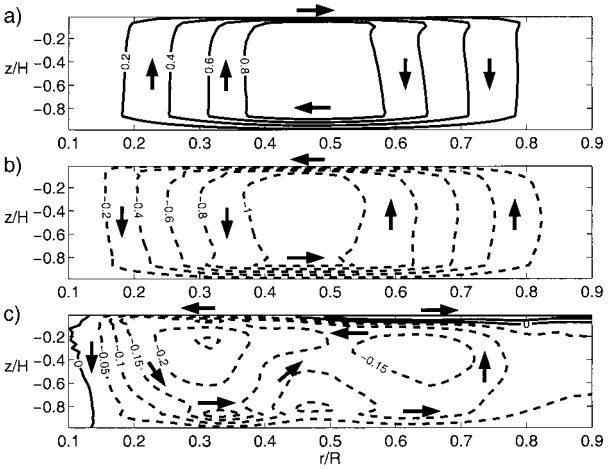

FIG. 11. (a) The mean streamfunction given by (1), (b) the eddy induced streamfunction given by (15), and (c) the residual circulation stream function given by (14), determined from the reference experiment and multiplied by r. Positive contours are solid: a clockwise circulation, negative contours are dashed: a counter-clockwise circulation). Streamfunctions have been normalized by the maximum of the mean streamfunction. Contour interval is 0.2 in (a) and (b) and 0.05 in (c).

In Figs. 11a and 11b we plot the mean wind-driven Eulerian circulation, Ψ_{Ek}, and the eddy-induced circulation, Ψ^*: to leading order they are in balance. This is just a different way of expressing the balance of terms seen in Figs. 8 and 9. In Fig. 11c, we plot the residual circulation. It consists of a large counterclockwise overturning cell that has an amplitude of only 20% of the Ekman transport. A small, surface trapped clockwise overturning circulation is also evident. At the surface, Ψ_{res} changes sign roughly where the buoyancy forcing changes sign. The major cell advects warm fluid upward and inward so that it can be cooled at the center. In the interior there is very little lateral motion and weak vertical circulation is associated with diapycnal fluxes. Under the cooling, the residual circulation fluxes buoyancy downwards to offset convection. Under the heating, the residual circulation fluxes buoyancy upwards to offset vertical diffusion. Furthermore, the no-flow conditions on the tank wall forces the residual circulation to be a closed, and hence, diabatic cell. In section 4 we discuss how changing the lateral boundary conditions to allow flow in and out of the domain, can allow a much stronger adiabatic residual circulation that resembles what is observed in the ACC.

b. Scaling analysis

Before discussing more detailed solutions, we first study the leading balances to yield simple formulas for the depth and strength of the front in terms of the surface

forcing—these were the central focus of Marshall et al. (2002).

At leading order we assume that the buoyancy flux, vertical diffusion and diapycnal terms are vanishingly small (see Fig. 9). Thus setting $B \to 0$, $\mu \to 1$, and $\kappa \to 0$ in (17), we find that the net advection of buoyancy must vanish and hence $\Psi_{\text{res}} \to 0$—as supported by Fig. 11. From (14), (15), and (11) with $\mu = 1$ the residual circulation is given by

$$\Psi_{\text{res}} = \frac{\tau}{f} + \frac{\overline{v'b'}}{\overline{b}_z}. \tag{18}$$

If Ψ_{res} vanishes, then

$$\frac{\tau}{f} = -\frac{[\overline{v'b'}]_{\epsilon=0}}{\overline{b}_z}, \tag{19}$$

where the subscript $\epsilon = 0$ indicates that this is the leading order eddy flux given by

$$[\overline{v'b'}]_{\epsilon=0} = -K_I \overline{b}_r. \tag{20}$$

At leading order, we assume that the eddy diffusivity takes on the constant interior value throughout the water column.

Equation (19) is the ''vanishing of the Deacon Cell'' and corresponds to the balance espoused by Johnson and Bryden (1989). Physically this may be interpreted as representing the transfer of momentum, imparted by the wind at the surface, through the column by ''eddy form drag'' (associated with the ''bolus'' flux $\overline{v'h'} = \overline{v'b'}/\overline{b}_z$). If the isopycnal slope, $s_\rho = -\overline{b}_r/\overline{b}_z$, scales like h_e/R, then (19) implies

$$K_I \frac{h_e}{R} \sim \frac{\tau_0}{f}, \tag{21}$$

where τ_0 is the scale of the wind stress.

At next order, we suppose that there *is* a buoyancy flux through the sea surface, so a nonzero Ψ_{res} develops to balance it, carrying heat from the heated region to the cooled region (see Fig. 11c). Assuming b scales like Δb and B like B_0 then (17) implies that

$$R\Psi_{\text{res}}\Delta b \sim R^2 B_0, \tag{22}$$

where we again assume that the diffusive and diapycnal terms on the right-hand side of (17) are negligible.

In order to continue we need a scaling for the residual circulation. The residual circulation develops because the eddy buoyancy flux increases toward the surface inducing a circulation that exceeds the Ekman transport. Advection by the resulting Ψ_{res} then balances the buoyancy flux through the surface. Substituting (19) into (14) gives

$$\Psi_{\text{res}} = \frac{[\overline{v'b'}]_{\epsilon=0}}{\overline{b}_z} - \frac{\overline{v'b'}}{\overline{b}_z} = (K - K_I)\frac{\overline{b}_r}{\overline{b}_z}. \tag{23}$$

Following the discussion in section 2c, we write

$$K - K_I = (1 + \epsilon)K_I - K_I = \epsilon K_I,$$

where ϵ is defined by (8). It then follows from (23) that the strength of the residual circulation is given by

$$\Psi_{\text{res}} \sim \epsilon K_I \frac{h_e}{R} \sim \epsilon \frac{\tau_0}{f}, \tag{24}$$

where (21) has been used. We see that Ψ_{res} is only a small fraction of the mean and eddy-induced circulation—our reference experiment gives $\epsilon \approx 0.1$—as supported by Fig. 11c.

Using (24) it follows from (22) that

$$\Delta b \sim \frac{B_0 f R}{\epsilon \tau_0} = \text{const} \times \frac{B_0}{w_E}, \tag{25}$$

where

$$w_E = \frac{\tau_0}{fR}$$

is a typical scale of the Ekman pumping. For a K_I given by (9), it follows using (10) and (4) that

$$K_I \sim \frac{c_e h_e \Delta b}{f} \tag{26}$$

and from (24), (25), and (26) that

$$h_e \sim \left(\frac{\epsilon}{c_e B_0 f}\right)^{1/2} \tau_0 = \text{const} \times \left(\frac{f}{B_0}\right)^{1/2} w_E R. \tag{27}$$

Formulas (25) and (27) have the same form as Eqs. (18) and (16) of Marshall et al. (2002). They will broadly account for the dependence of h_e and Δb on external parameters found in our explicit solutions, described below.

c. Buoyancy budget model

We can derive a more detailed mathematical model of the stratification by examining the horizontal and vertical buoyancy budgets discussed in section 2 (see Figs. 8 and 9). We use the buoyancy (4), the eddy parameterization (9), and the eddy fluxes (see section 2c) to construct a system that can be solved for the e-folding depth h_e and horizontal structure $M(r)$ of the front. The details of the model are given in the appendix.

The model takes as input the surface forcing—the strength and form of the wind stress and buoyancy forcing—and requires the specification of three parameters: the buoyancy at the center of the tank $b_{r=0}$, the increase in lateral eddy flux at the surface ϵ, and the eddy efficiency c_e.

For each simulation, the parameter $b_{r=0}$ in (6) is set to the value diagnosed from the simulation. The coefficient c_e is held constant and set equal to 0.043 as suggested by Fig. 10. The parameter ϵ is tuned to obtain the best fit and yields an optimal value of

$$\epsilon = 0.10. \tag{28}$$

The increased eddy diffusivity in the mixed layer results

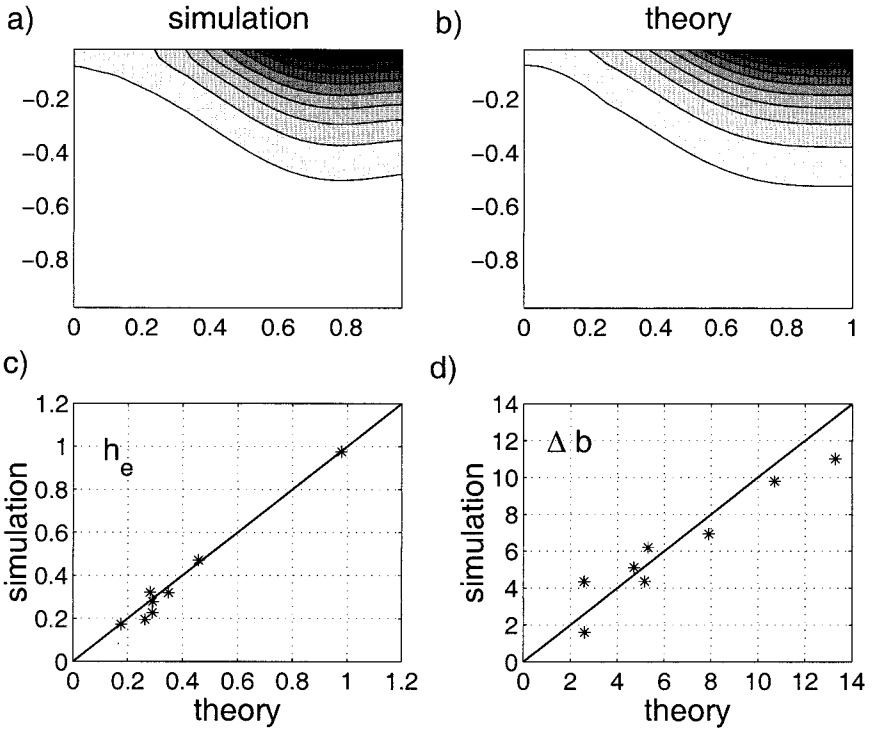

FIG. 12. Plots comparing the numerical simulations and theoretical predictions. (a) The stratification of the reference simulation and (b) that predicted by theory. (c) and (d) h_e and Δb plotted as diagnosed for the simulation vs that predicted by the theory. The stars are the data; the line indicates a perfect match. The depth h_e is normalized by H and the strength Δb by $b_{r=0}$.

in a 10% increase in the lateral buoyancy flux and so the residual circulation is roughly 10% of the mean circulation.

In Fig. 12 we plot the contours of the buoyancy from the reference numerical experiment (a) and as predicted by the theory (b). Clearly its essential form has been captured. We also plot values of the *e*-folding scale h_e (c) and the buoyancy strength Δb (d) as diagnosed from the simulation versus the value calculated from the theory. The points lie along a straight line, indicating that the theory is capturing the dependence of the stratification on the varying forcing.

4. Using the theory to make predictions

a. Application to ACC

Having established that our theory can broadly explain the results of our numerical simulations, we apply our model to the ACC. Obviously, the dynamics of the ACC involve many complications that are not present in either our numerical simulations or theory. Here, we wish only to determine whether our theory can predict a plausible stratification and depth scale for the ACC.

Typical parameter values for the ACC are

$$\tau_s = 0.2 \text{ N m}^{-2}, \qquad \rho_{\text{ref}} = 1030 \text{ kg m}^{-3},$$
$$R = 2500 \text{ km}, \qquad H = 4500 \text{ m},$$
$$B_0 = 5 \times 10^{-9} \text{ m}^2 \text{ s}^{-3}, \qquad \kappa = 1.5 \times 10^{-5} \text{ m}^2 \text{ s}^{-1},$$
$$f = 1.2 \times 10^{-4} \text{ s}^{-1}, \qquad b_{r=0} = 5 \times 10^{-3} \text{ m s}^{-2},$$

while we hold c_e and ϵ to the values given above. In the above, τ_s is the scale of the wind stress, the scale of the wind stress per unit density is

$$\tau_0 = \tau_s/\rho_{\text{ref}} = 1.9 \times 10^{-4} \text{ m}^2 \text{ s}^{-2}$$

so that

$$w_E = \frac{\tau_0}{fR} = 7.9 \times 10^{-7} \text{ m s}^{-1}.$$

The Ekman pumping scale is equivalent to an average pumping velocity of -25 m yr^{-1}. Assuming a thermal expansion coefficient of 1×10^{-4} K^{-1}, the buoyancy flux corresponds to an average cooling of 20 W m^{-2} south of the Polar Front at 60°S. The surface buoyancy flux pattern (see Fig. 3) and typical scale of the flux chosen here are at best a crude guess at the actual surface flux forcing the ACC. We discuss the complex nature of the observed surface buoyancy flux and possible implications in the conclusions.

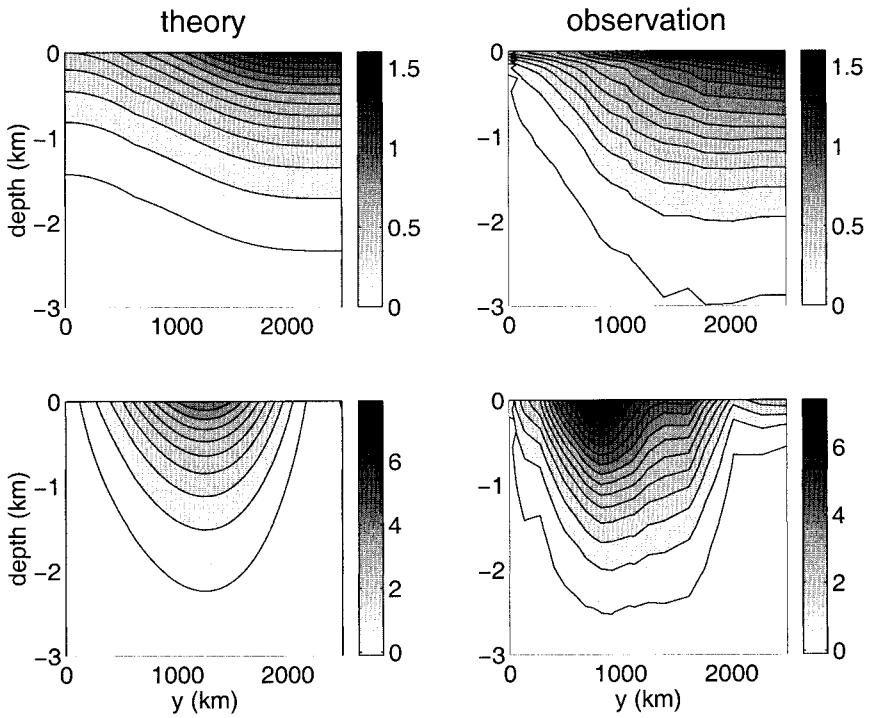

FIG. 13. Contours of the buoyancy (upper plot in cm s^{-2}) and thermal wind current (lower plot in cm s^{-1}) as predicted by the theory with forcing typical of the ACC (left) and from Levitus and Boyer (1994; right).

The theory predicts the Polar Front and thermal wind current shown in Fig. 13. The front has

$$h_e = 1040 \text{ m}, \qquad \Delta b = 7.3 \times 10^{-3} \text{ m s}^{-2},$$

corresponding to a temperature jump of 7.4°C. The associated thermal wind current has a maximum velocity of 5 cm s^{-1} with a transport of 62 Sv (Sv $\equiv 10^6$ m^3 s^{-1}). In Fig. 13 we have also plotted the alongstream averaged buoyancy and corresponding thermal wind velocity as calculated from the hydrological data (Levitus and Boyer 1994). The transport of the thermal wind is roughly 100 Sv. Although the depth of the front is reasonable, the velocity and transport of the current are somewhat lower than than observed in the ACC. The ACC is a much sharper front than our model predicts, increasing the velocity and transport. This is a consequence of the fact that the *e*-folding depth of the ACC is not constant but increases as one travels northward. Yet, that the predicted stratification and flow of the ACC are within a factor of 2 of observations lends credence to our belief that our numerical simulation and theory is describing the leading order process that establishes the ACC. We discuss how these features may be altered by other effects—the β plane, topography, etc.—in the conclusions.

b. Variations in forcing

How, according to our theory, does the stratification and flow of a circumpolar current change when the magnitude of the wind stress τ_s and buoyancy flux B_0 are varied? We will use the ''typical'' ACC parameter values given above as our reference state.

In Figs. 14a and 14b, we plot h_e and Δb versus τ_s, all other parameters being held constant at their reference values. For high wind stress, the front deepens linearly with wind stress while the strength varies inversely to the wind stress, exactly as predicted by (27) and (25); the dashed lines in Figs. 14a and 14b represent the formulas in (27) and (25). For low wind stress we enter the diffusive regime (see appendix) in which both the depth and the strength of the front increase, but with only a weak dependence on the wind stress.

In Figs. 14c and 14d we plot h_e and Δb versus B_0, all other parameters being held constant at their reference values. The depth decreases as the surface forcing increases and is much more sensitive to changes in the forcing when it is weak. The strength of the front increases linearly with the forcing, again in accord with (25) and (27).

Having obtained the stratification of the front, we can easily obtain the transport of the associated thermal wind current. The baroclinic transport of the current is

$$T_{\text{bc}} = \int_{-H}^{0} \int_{0}^{R} \overline{u}\, dr\, dz$$

$$= \frac{h_e^2 \Delta b}{f}\left[1 - \left(1 + \frac{H}{h_e}\right)\exp\left(-\frac{H}{h_e}\right)\right], \qquad (29)$$

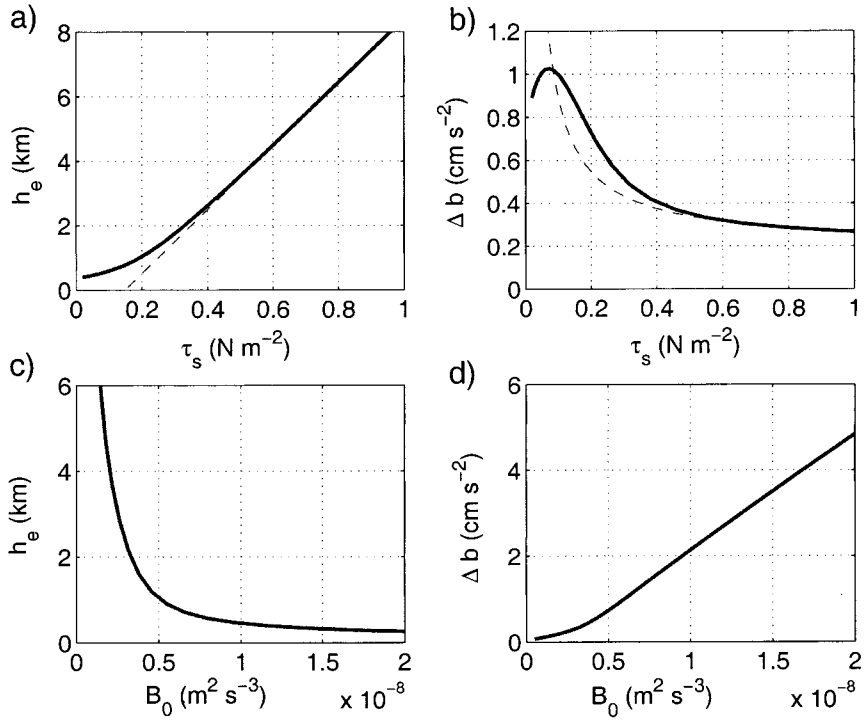

FIG. 14. Plots of (a) the frontal depth h_e and (b) the strength Δb vs wind stress for fixed B_0 and f. The dashed curves are given by (27) and (25). Plots of (c) h_e and (d) Δb vs the surface buoyancy flux for fixed τ_s and f.

where (4) has been used. The baroclinic transport can be expressed in terms of the stratification—the e-folding depth h_e and the meridional buoyancy anomaly Δb. Note that, if the leading order balance between the wind stress and eddy flux holds [i.e. (21)] and the eddy parameterization holds [i.e. (26)], then it follows that

$$T_{\rm bc} \sim \frac{\tau R}{c_e f}; \tag{30}$$

the transport varies linearly with the wind stress.

In Fig. 15 we show log–log plots of the baroclinic transport predicted by the theory versus the wind stress (a) and the buoyancy forcing (b). For high wind stresses, $\tau_s > 0.1$ N m^{-2}, the transport varies linearly with the wind stress, as suggested by (30). The transport does vary with buoyancy forcing—for typical ACC values, the transport decreases like the square root of the buoyancy forcing. Similarly, for low wind stress, the transport does not depend linearly on wind stress. This suggests that the leading order balance of winds and eddy fluxes that gives (30) is not solely responsible for determining the transport and that this balance breaks down as either the winds decrease or the buoyancy forcing increases. For very strong winds or weak surface forcing, the current is very deep (see Fig. 14) and the finite depth of the domain restricts the transport [see (29)].

How do these predictions compare with those of other investigators? Johnson and Bryden (1989) suggested the transport varies like the square root of the wind stress, while Straub (1993) suggested the transport is independent of the wind stress. The two-layer simulations of Tansley and Marshall (2001) suggested that both could hold, the former for strong wind stresses and the latter

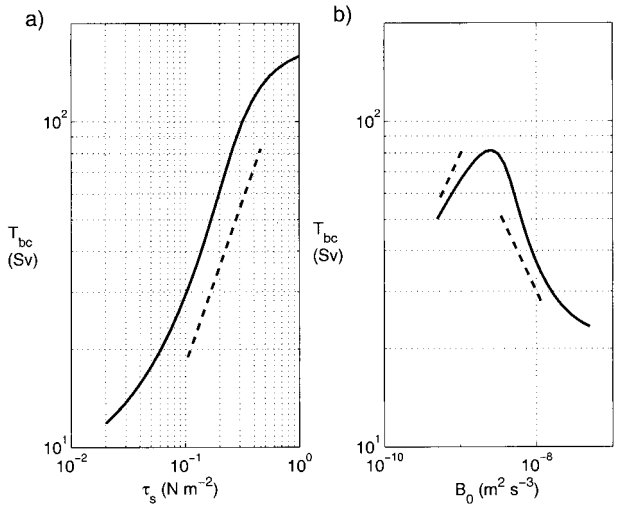

FIG. 15. Log–log plots of the baroclinic transport as predicted by the theory vs wind stress (a) and surface buoyancy forcing (b). The dashed lines show a slope of one in (a) and $-1/2$ and $1/2$ in (b).

for weak wind stresses. However, all these studies assume that the stratification is known a priori and do not consider buoyancy effects. Recent simulations by Gnanadesikan and Hallberg (2000) using a two-layer model, which parameterized diapycnal fluxes in terms of a vertical velocity, resulted in an ACC with a transport that varied linearly with the wind stress. Though their balance is somewhat different from ours, they recognize that changing the wind stress changes the structure of the Polar Front, particularly the depth and lateral density gradients, just as described here.

c. ACC residual circulation

To complete our discussion of the application of our results to the ACC, we return to the residual circulation, which redistributes tracers in the meridional plane and establishes how they are subducted from the surface. It also controls the transformation of water masses, determining the rate at which water is brought to the surface to be transformed by exposure to air–sea fluxes. As such, it is essential in determining the role of the Antarctic region in the thermohaline circulation.

We consider (17) in the limit most likely relevant to the ocean where diffusion and diapycnal eddy fluxes are negligible, giving

$$J(\Psi_{\text{res}}, b) = \frac{\partial B}{\partial z}. \tag{31}$$

For application to the ocean we will work in a cross-stream coordinate, y, so that $J(\Psi_{\text{res}}, b) = (\Psi_{\text{res}})_y b_z - (\Psi_{\text{res}})_z b_y$.

If we consider (17) in the mixed layer, where vertical gradients of buoyancy vanish, then we have

$$-\frac{\partial \Psi_{\text{res}}}{\partial z}\frac{\partial b_m}{\partial y} = \frac{\partial B}{\partial z},$$

where $b_m(y)$ is the mixed layer buoyancy. Integrating over the depth of the mixed layer gives

$$\Psi_{\text{res}}(z = -h_m)\frac{\partial b_m}{\partial y} = B, \tag{32}$$

where B is the surface buoyancy flux. This result can also be obtained by considering the budget of buoyancy between two isopycnals following Marshall (1997). The residual circulation is forced locally by the surface buoyancy flux. If, for example, the mixed layer buoyancy gradient is constant, the residual circulation will be directly proportional to the surface buoyancy flux at each latitude. We see this structure at the surface in Fig. 11c with a negative residual circulation under the cooling and a positive residual circulation under the heating.

For scales typical of the ACC given in section 4a, one can estimate the strength of the residual circulation using (22) to get

$$\Psi_{\text{res}} \sim 0.94 \text{ m}^2 \text{ s}^{-1}.$$

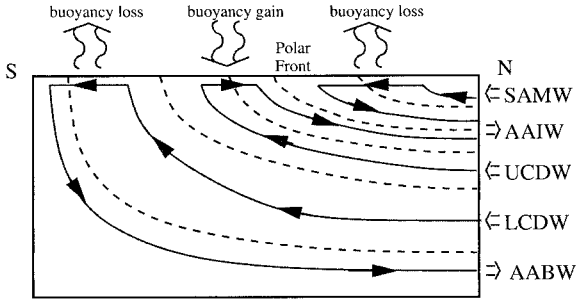

FIG. 16. A sketch of the diabatic Deacon cells driven by surface buoyancy fluxes. Three cells are driven by buoyancy loss north of the Polar Front, buoyancy gain south of the Polar Front, and weak buoyancy loss in the far south near Antarctica. In the southern cell, LCDW upwells loses buoyancy at the surface and subducts to form AABW. In the central cell, UCDW upwells gains buoyancy at the surface and subducts to form AAIW. In northern cell, SAMW upwells and loses buoyancy at the surface and subducts to form AAIW.

The net transport by the residual circulation over the length of the ACC (~20 000 km) is then of order 18.8 Sv, consistent with the analysis of Marshall (1997), which found residual circulations of 10–15 Sv. Compared to the zonal transport (~100 Sv), this flow is weak. However, it is sufficient to supply, for example, 30–40 Sv of estimated southward transport of deep water across the circumpolar zone.

Below the mixed layer the buoyancy forcing vanishes, so

$$J(\Psi_{\text{res}}, b) = 0, \tag{33}$$

implying that the residual circulation is directed along isentropic surfaces in the interior. That is, unlike our numerical simulation where the interior residual circulation was diabatic, we expect the interior residual circulation for the ACC to be adiabatic. Furthermore, the northern boundary of the ACC is open to exchanges with the oceans, and therefore allows the residual circulation to transports buoyancy in and out of the ACC region to balance any net surface flux.

The simple surface buoyancy forcing adopted in our numerical experiments is not supported by all observations. For example, Speer et al. (2000), using Comprehensive Ocean–Atmosphere Data Set data and an inverse model, argue that the ocean loses buoyancy north of the ACC. The region of buoyancy gain is shifted to the south of the Polar Front and is enhanced by freshwater sources from ice melt. Around Antarctica heat loss and fluxes of salt from brine rejection as ice forms compete with freshwater sources as ice melt. Their estimates suggest a weak buoyancy loss in the region. The resulting residual circulation from such a scenario is sketched in Fig. 16.

The two regions of surface buoyancy loss drive a residual circulation cell that pulls relatively buoyant water to the surface where it loses buoyancy to the atmosphere as it travels southward and subsequently subducts. Conversely, the surface gain of buoyancy pulls

less buoyant water to the surface where it gains buoyancy from the atmosphere as it travels northward and subsequently subducts. In terms of the ACC nomenclature, the southern most cell represents the upwelling of Lower Circumpolar Deep Water (LCDW) and its transformation into Antarctic Bottom Water (AABW). The central cell represents the upwelling of Upper Circumpolar Deep Water (UCDW) and its transformation into Antarctic Intermediate Water (AAIW). And the northern cell represents the upwelling of Subantarctic Mode Water (SAMW) and its transformation into AAIW. Such a scenario is discussed in more detail in Marshall (1997) and Speer et al. (2000).

Our approach here is a somewhat simplistic view of the complicated meridional circulations that play a role in water transformation across the ACC. Further details of the water signatures and heat and salt transformations must be considered to complete the complicated transformation process that closes the thermohaline circulation (see Bryden and Cunningham 2001; Speer et al. 2000 for further discussion). However, it should be noted that the dynamical framework set out here is in accord with their descriptions.

5. Conclusions

In this paper we have examined the nonlinear interaction of surface forcing, eddies, and stratification within the context of a circumpolar current. We have described numerical simulations investigating how an initially homogeneous fluid responds to a combination of both thermal and mechanical surface forcing. The forcing mimics that found in the Southern Ocean: cooling at the pole and heating in the subtropics with a zonal wind stress driving a meridional overturning. Such forcing creates a baroclinically unstable Polar Front in which the resulting eddies sweep heat across the front from the warm subtropics to the polar region. When the eddy heat transport balances the surface forcing, a statistically steady state is achieved. The resulting front supports a current, in thermal wind balance with the sloping isopycnals, which we adopt as a simple analogue to the ACC.

Adopting a TEM framework, we proceeded to develop a theory that predicts the lateral structure and depth of the front and the sense of the residual circulation given the strength and form of the forcing. By examining the buoyancy budgets we showed that, at zero order, circulation driven by eddies balances the mean wind driven transport (Figs. 8, 9, and 11). At next order the residual circulation transports buoyancy across the front to balance air–sea fluxes (see Fig. 11c). This is our dynamical interpretation of the diabatic Deacon cell found in the observations in Speer et al. (2000).

In the advective regime (see appendix), the depth of the front varies linearly with the wind stress and inversely with the square root of the buoyancy forcing [see (27)]. Conversely, the strength of the front varies linearly with the buoyancy forcing and inversely with the wind stress [see (25)]. The net baroclinic transport varies linearly with wind stress and inversely with the square root of the buoyancy forcing (see Fig. 15). The present ACC is probably in the advective regime, with diapycnal fluxes playing only a small role except in the surface mixed layer. However, relatively small changes in the forcing can move our model of the circumpolar current into a diffusive regime (see appendix) where the wind stress becomes less important in determining the structure of the front and current.

Despite the idealized nature of our numerical experiments, we believe the balances highlighted here are important in the dynamics of the ACC. The leading order balance between eddies and wind driven overturning has been recognized in numerical models as a weakening or vanishing of the Deacon Cell (Döös and Webb 1994; Danabasoglu et al. 1994). It has also been supported by analysis of eddy fluxes calculated from mooring data (Johnson and Bryden 1989; Phillips and Rintoul 2000), altimetry (Keffer and Holloway 1988), and eddy-resolving numerical models with realistic topography (Ivchenko et al. 1996; Gille 1997).

It is clear from our examination here, that the buoyancy forcing plays a critical role in the dynamics of the ACC. Unfortunately, surface buoyancy budgets in the Southern Ocean are poorly observed and understood. Not only must heat fluxes and $E - P$ be considered, but the ACC is also a region of large salinity fluxes associated with ice formation and melt (see discussion in Speer et al. 2000). With our simple surface buoyancy forcing and geometry, we generate a residual circulation with a single overturning cell that transports buoyancy polewards. But, by taking advantage of the TEM formulation, we are able to connect our idealized simulations and analysis to a more realistic description of the ACC. With an adiabatic interior, the surface forcing generates multiple diabatic Deacon cells, each associated with the transformation of water masses (see Fig. 16). Such cells play an essential role in closing the thermohaline circulation by transforming UCDW into AAIW (see Marshall 1997; Speer et al. 2000).

A key absence from our theory is the stabilizing influence of a β plane. Intuitively, one might expect the β plane to inhibit eddy transport and result in a deeper front. Since the transport grows like the square of the depth and if the effect of β were to increase the depth by only 30%, the transport would roughly increase to 100 Sv—within the range of observed values. It is not nearly so simple to predict how the topography that the ACC traverses will affect the stratification. Marshall (1995), Gille (1997), Gnanadesikan and Hallberg (2000), and Tansley and Marshall (2001) (among many others) have illustrated the importance of the constrictions imposed by Drake Passage and bottom topography in influencing not only the path of the ACC but the formation of the eddies. The connection of topography and eddy fluxes is essential if momentum is to be dis-

sipated through the form drag scenario of Munk and Palmén (1951) mentioned above. Such changes, obviously, modify the details of the buoyancy budgets discussed here. As such, this remains an active area of research.

Finally, the ACC does not exist in isolation. Its interaction with subtropical gyres, western boundary currents, and the flow and deep-water formation in the seas around Antarctica will no doubt influence its structure. The many complications in examining the influences on the ACC when it is modeled as part of the global ocean circulation can be seen in the recent work of Gent et al. (2001).

While we continue to adapt our model, we are also taking advantage of the growing database of satellite observations to examine the balances proposed here and predict the implied residual circulation. We believe that through a combination of idealized studies like that presented here, detailed numerical modeling, and continued analysis of observations we will be able to identify and understand the processes that control the ACC.

Acknowledgments. We thank the Physical Oceanography division of the National Science Foundation whose support made this study possible. R.H.K. was supported by an NSERC PDF.

APPENDIX

Details of Analytical Model

In this appendix we describe the derivation and method of solution of an analytical model of the front that calculates its lateral and vertical stratification given patterns of surface forcing.

a. Buoyancy budgets

Following Marshall et al. (2002), we begin by formulating the balances illustrated in Figs. 8 and 9 as mathematical equations. Integrating (13) over the cylinder of radius r shown in Fig. 8 gives the horizontal budget equation

$$2\pi r \int_{-H}^{0} (\overline{v}\,\overline{b} + \overline{v'b'})\, dz = 2\pi \int_{0}^{r} B(\xi)\xi\, d\xi. \quad \text{(A1)}$$

Integrating (13) over the disc shown in Fig. 9 gives the vertical budget equation,

$$\int_{0}^{R} \left(\overline{w}\,\overline{b} + \overline{w'b'} - \kappa \frac{\partial \overline{b}}{\partial z} \right) r\, dr = 0. \quad \text{(A2)}$$

Using (2) with (1), (7), and (4) reduces (A1) to

$$a_1 \frac{dM}{dr} + a_2 \frac{\tau(r)}{f_0} M = -\mathcal{B}, \quad \text{(A3)}$$

where

$$\mathcal{B}(r) = \frac{1}{r} \int_{0}^{r} B(\xi)\xi\, d\xi \quad \text{(A4)}$$

and $a_{1,2}$ are constant in r and given by

$$a_1 = \int_{-H}^{0} K(z) \exp(z/h_e)\, dz, \quad \text{(A5)}$$

$$a_2 = \int_{-H}^{0} \mathcal{E}(z) \exp(z/h_e)\, dz. \quad \text{(A6)}$$

Following the discussion in section 2c and expanding the integrals we obtain

$$a_1 = (1 + \epsilon) K_I h_e [1 - \exp(-H/h_e)],$$

where ϵ is given by (8) and

$$a_2 = 1 - \exp(-H/h_e),$$

where it has been assumed that the Ekman layers are thin relative to the e-folding depth. Then the solution to (A3) is

$$M(r) = M(0) - \frac{1}{a_1} \int_{0}^{r} \exp[I(\xi) - I(r)] \mathcal{B}(\xi)\, d\xi, \quad \text{(A7)}$$

where

$$I(r) = \frac{a_2}{a_1 f_0} \int_{0}^{r} \tau(\xi)\, d\xi. \quad \text{(A8)}$$

Similarly, the vertical balance (A2) reduces to

$$\int_{0}^{R} \left[\frac{\tau}{f_0} \frac{dM}{dr} - \frac{K_I h_e}{M} \left(\frac{dM}{dr} \right)^2 + \frac{\kappa}{h_e} M \right] r\, dr = 0, \quad \text{(A9)}$$

where we have assumed that we are below the Ekman layer and mixed layer so that we can ignore the vertical structure of ϵ, K, and set $\mu = 1$.

From (9), (10), and (4) it follows that

$$K_I = c_e \frac{h_e \Delta b}{f} \left[1 - \exp\left(-\frac{H}{h_e} \right) \right], \quad \text{(A10)}$$

where Δb is given by (5).

The model consists of three equations, the horizontal buoyancy budget which determines the horizontal structure through (A7), the vertical buoyancy budget (A9), and the definition of the strength of the front, Δb, given by (5). These equations are nonlinearly coupled through (A10).

b. Method of solution

We define the functions

$$F(h_e, \Delta b) = \int_{0}^{R} \left[\frac{\tau}{f_0} \frac{dM}{dr} - \frac{K_I h_e}{M} \left(\frac{dM}{dr} \right)^2 + \frac{\kappa}{h_e} M \right] r\, dr, \quad \text{(A11)}$$

$$G(h_e, \Delta b) = \Delta b - M(R) + M(0), \quad \text{(A12)}$$

where $M = M(r; h_e, \Delta b)$ and M' are given by (A7) and

(A3), respectively. The integral in (A11) is evaluated using MATLAB's integral function *quad*8. The solution, the values of h_e and Δb such that (5) and (A9) are satisfied, is given by the roots of functions G and F:

$$G(h_e, \Delta b) = F(h_e, \Delta b) = 0.$$

These are solved using MATLAB's root finding function *fzero*. Given a reasonable first guess, typically 10 to 100 iterations are required to converge to a solution accurate to several significant digits.

The parameters $M(0)$, c_e, and ϵ must be given to determine a solution. For comparison to the numerical simulations the $M(0)$ was diagnosed from the each simulation, $c_e = 0.043$ (see Fig. 10), and ϵ is chosen so that the solutions best fit the simulations.

c. Diapycnal advection and diffusion

In section 4, we assumed that diffusion was negligible and determined a scaling for the depth and strength of the front—see (25) and (27). Variations in ACC parameters seen in Fig. 14 are largely in accord with this simple scaling. However, when diffusion is included in the theoretical solutions, they depart from these simple scalings for some choices of wind and buoyancy forcing. In this appendix we examine the balance between diapycnal fluxes—eddy advection and diffusion—and surface buoyancy flux. In so doing we derive a measure for when diffusion is important and scales for the depth and strength of the front when diffusion dominates diapycnal advection.

The leading order balance in (A3) and (A9) is between eddy flux and the mean wind-driven transport (see Figs. 8 and 9). To get an equation that describes the secondary balance, between diapycnal terms on the left hand side of (17), we simply use (A3) to replace the eddy term in (A9) to get

$$\int_0^R \left[\left(\frac{\epsilon}{1+\epsilon}\right)\frac{\tau}{f}\frac{dM}{dr} + \frac{K_I h_e}{a_1}\frac{\mathcal{B}}{M}\frac{dM}{dr} + \frac{\kappa}{h_e}M\right] r\, dr = 0.$$

Integrating the first term by parts gives

$$\int_0^R \left[\left(\frac{\epsilon}{1+\epsilon}\right)\overline{w} - \frac{\kappa}{h_e}\right] Mr\, dr = \frac{K_I h_e}{a_1}\int_0^R \frac{\mathcal{B}}{M}\frac{dM}{dr} r\, dr. \quad \text{(A13)}$$

Now we have a balance between diapycnal advection (first term on lhs), diffusion (second term on lhs) and surface buoyancy forcing (rhs).

In (A13), a combination of the diapycnal advection and diffusion must balance the buoyancy forcing. This leads to two scaling regimes, one where advection dominates and one where diffusion dominates. The transition between them is clearly illustrated in Fig. A1 where we plot the two terms on the left of (A13) as a function of wind stress τ_s. As the wind stress increases, we move from a regime dominated by diffusion to one dominated by advection.

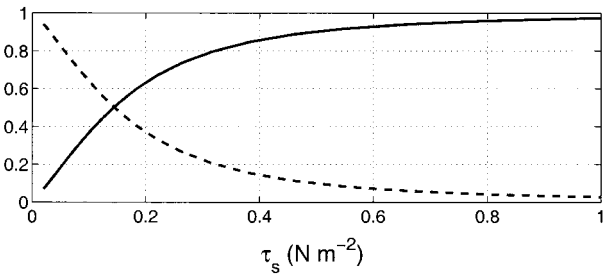

FIG. A1. Plots of the diapycnal advection (solid line) and the diffusion (dashed line)—the two terms on the left of (A13)—as the wind stress varies. The values have been normalized by the term on the right of (A13) so that the two curves sum to one.

We now examine the depth and strength of the front in these two regimes, assumming that $h_e \ll H$ so that $\exp(-H/h_e) \to 0$. The leading order balance between the eddy fluxes and the mean Ekman transport as discussed in the text (see section 3b); that is,

$$\frac{K_I h_e}{R} \sim w_E R. \quad \text{(A14)}$$

If we assume that diapycnal advection dominates the diffusion in (A13),

$$\frac{\epsilon}{1+\epsilon} w_E \gg \frac{\kappa}{h_e}, \quad \text{(A15)}$$

then the diapycnal advection balances the heating, and (A13) implies

$$\epsilon w_E \Delta b \sim B_0. \quad \text{(A16)}$$

Relations (A14) and (A16) are equivalent to those found in section 3b and can be rearranged to give the formulas for Δb and h_e given by (25) and (27), respectively. Given (27) we can rewrite (A15) to get

$$w_E \gg \left[\frac{(1+\epsilon)^2 c_e}{\epsilon^3}\right]^{1/4}\left(\frac{\kappa}{R}\right)^{1/2}\left(\frac{B_0}{f_0}\right)^{1/4} \equiv w_c. \quad \text{(A17)}$$

Thus, w_c gives us a critical pumping that delineates between the regime dominated by diapycnal eddy fluxes and the regime dominated by diffusion. Note that this critical pumping value depends on the buoyancy forcing, increasing as the buoyancy forcing increases and thus moving towards the diffusive regime.

For typical numbers of the ACC, the wind stress corresponds to an Ekman pumping velocity scale of

$$w_0 = 7.9 \times 10^{-7}\ \text{m s}^{-1}.$$

Calculating the critical value of the pumping we get

$$w_c = 7.5 \times 10^{-7}\ \text{m s}^{-1},$$

indicating that the ACC exists in the regime where advection is greater than diffusion. Figure A1 indicates that at $\tau_s = 0.2$, the advective term is larger than dif-

fusive term, but it also illustrates that a small reduction in wind stress moves the ACC into a regime where diapycnal advection and diffusion contribute equally.

If the pumping is weak,

$$\frac{\epsilon}{1+\epsilon} w_E \ll \frac{\kappa}{h_e}, \tag{A18}$$

the diapycnal advection is dominated by the diffusion. Now, diffusion balances the buoyancy flux term in (A13), implying that

$$\frac{\kappa \Delta b}{h_e} \sim \frac{B_0}{1+\epsilon}. \tag{A19}$$

Combining (A19) with (A14) and using (A10) gives

$$\Delta b \sim \left(\frac{1+\epsilon}{c_e} \frac{f_0 B_0^2 w_E R^2}{\kappa^2} \right)^{1/3},$$

$$h_e \sim \left[\frac{1}{(1+\epsilon)^2 c_e} \frac{f_0 \kappa w_E R^2}{B_0} \right]^{1/3}.$$

In the diffusive regime, the depth and the strength of the front grow slowly with increasing wind stress as seen in Fig. 14 when the wind stress is low.

Furthermore, if the wind stress is very weak the leading order balance between winds and eddy fluxes may break down, with the eddy flux balancing the surface buoyancy flux. However, while this limit may help explain the behavior in Fig. 14, and 15 at low τ_s or high B_0, we do not believe that it is relevant to realistic ocean dynamics.

REFERENCES

Andrews, D. G., and M. E. McIntyre, 1976: Planetary waves in horizontal and vertical shear: the generalized Eliassen–Palm relations and the mean zonal acceleration. *J. Atmos. Sci.,* **33,** 2031–2048.

——, J. Holton, and C. Leovy, 1987: *Middle Atmosphere Dynamics.* Academic Press, 489 pp.

Danabasoglu, G., J. C. McWilliams, and P. Gent, 1994: The role of mesoscale tracer transport in the global ocean circulation. *Science,* **264,** 1123–1126.

Döös, K., and D. Webb, 1994: The Deacon Cell and other meridional cells of the Southern Ocean. *J. Phys. Oceanogr.,* **24,** 429–442.

Gent, P. R., W. G. Large, and F. O. Bryan, 2001: What sets the mean transport through the Drake Passage? *J. Geophys. Res.,* **106,** 2693–2712.

Gille, 1997: The Southern Ocean momentum balance: Evidence for topographic effects from numerical model output and altimeter data. *J. Phys. Oceanogr.,* **27,** 2219–2231.

Gnanadesikan, A., and R. W. Hallberg, 2000: On the relationship of the Circumpolar Current to Southern Ocean winds in course-resolution ocean models. *J. Phys. Oceanogr.,* **30,** 2013–2034.

Held, I. M., and T. Schneider, 1999: The surface branch of the zonally averaged mass transport circulation in the troposphere. *J. Atmos. Sci.,* **56,** 1688–1697.

Ivchenko, V. O., K. J. Richards, and D. P. Stevens, 1996: The dynamics of the Antarctic Circumpolar Current. *J. Phys. Oceanogr.,* **26,** 753–774.

Johnson, G. C., and H. L. Bryden, 1989: On the size of the Antarctic Circumpolar Current. *Deep-Sea Res.,* **36,** 39–53.

Jones, H., and J. Marshall, 1997: Restratification after convection. *J. Phys. Oceanogr.,* **27,** 2276–2287.

Keffer, T., and G. Holloway, 1988: Estimating Southern Ocean eddy flux of heat and salt from satellite altimetry. *Nature,* **332,** 624–626.

Killworth, P. D., 1992: An equivalent-barotropic mode in the Fine Resolution Antarctic Model. *J. Phys. Oceanogr.,* **22,** 1379–1387.

Krupitsky, A., V. M. Kamenkovich, N. Naik, and M. A. Cane, 1996: A linear equivalent barotropic model of the Antarctic Circumpolar Current with realistic coastlines and bottom topography. *J. Phys. Oceanogr.,* **26,** 1803–1824.

Levitus, S., and T. Boyer, 1994: *World Ocean Atlas 1994.* Vol. 4: *Temperature,* NOAA Atlas NESDIS 4, 117 pp.

Marshall, D., 1995: Topographic steering of the Antarctic Circumpolar Current. *J. Phys. Oceanogr.,* **25,** 1636–1650.

——, 1997: Subduction of water masses in an eddying ocean. *J. Marine Res.,* **55,** 201–222.

Marshall, J., 1981: On the parameterization of geostrophic eddies in the ocean. *J. Phys. Oceanogr.,* **11,** 257–271.

——, D. Olbers, H. Ross, and D. Wolf-Gladrow, 1993: Potential vorticity constraints on the dynamics and hydrography of the Southern Ocean. *J. Phys. Oceanogr.,* **23,** 465–487.

——, A. Adcroft, C. Hill, L. Perelman, and C. Heisey, 1997a: A finite-volume, incompressible Navier Stokes model for studies of the ocean on parallel computers. *J. Geophys. Res.,* **102** (C3), 5753–5766.

——, C. Hill, L. Perelman, and A. Adcroft, 1997b: Hydrostatic, quasi-hydrostatic, and nonhydrostatic ocean modeling. *J. Geophys. Res.,* **102** (C3), 5733–5752.

——, H. Jones, R. H. Karsten, and R. Wardle, 2002: Can eddies set ocean stratification? *J. Phys. Oceanogr.,* **32,** 26–38.

McWilliams, J. C., W. R. Holland, and J. S. Chow, 1978: A description of numerical Antarctic Circumpolar Currents. *Dyn. Atmos. Oceans,* **2,** 213–291.

Munk, W. H., and E. Palmén, 1951: Note on the dynamics of the Antarctic Circumpolar Current. *Tellus,* **3,** 53–55.

Pedlosky, J., 1987: *Geophysical Fluid Dynamics.* 2d ed. Springer-Verlag, 710 pp.

Phillips, H. E., and S. R. Rintoul, 2000: Eddy Variability and Energetics from Direct Current Measurements in the Antarctic Circumpolar Current South of Australia. *J. Phys. Oceanogr.,* **30,** 3050–3076.

Speer, K., S. R. Rintoul, and B. Sloyan, 2000: The diabatic Deacon cell. *J. Phys. Oceanogr.,* **30,** 3212–3222.

Straub, D. N., 1993: On the transport and angular momentum balance of channel models of the Antarctic Circumpolar Current. *J. Phys. Oceanogr.,* **23,** 776–782.

Tansley, C. E., and D. Marshall, 2001: On the dynamics of wind-driven circumpolar currents. *J. Phys. Oceanogr.* **31,** 3258–3273.

Treguier, A. M., I. M. Held, and V. D. Larichev, 1997: On the parameterization of the quasigeostrophic eddies in primitive equation ocean models. *J. Phys. Oceanogr.,* **27,** 567–580.

Visbeck, M., J. Marshall, and H. Jones, 1996: Dynamics of isolated convective regions in the ocean. *J. Phys. Oceanogr.,* **26,** 1721–1734.

Whitehead, J., J. Marshall, and G. Hufford, 1996: Localised convection in rotating stratified fluid. *J. Geophys. Res.,* **101** (C10), 25 705–25 721.